A Facile Route to Aqueous Phase Synthesis of Mesoporous Alumina with Controllable Structural Properties

Wei Wu, Zhijian Wan, Mingming Zhu and Dongke Zhang*

Centre for Energy (M473)

The University of Western Australia

35 Stirling Highway, Crawley, WA 6009, Australia

(A manuscript offered to ***Microporous and Mesoporous Materials***)

*corresponding author:

Email: Dongke.Zhang@uwa.edu.au

Phone: 61-8-6488 7600

Fax: 61-8-6488 7622

Abstract

Mesoporous aluminas (MAs) with tunable structural properties, including BET surface area, pore volume and pore size, were successfully synthesized based on a sol-gel process via hydrolysis of aluminium isopropoxide associated with a structure-directing agent (SDA) as template in an acidic aqueous system. The effect of template type, template addition amount and inorganic aluminium precursor doping on the structural properties of the resulting MAs were systematically investigated. Four templates, including two non-ionic triblock copolymers P123 and F127, an amine based cationic quaternary surfactant cetyltrimethylammonium bromide (CTAB) and an anionic surfactant sodium dodecyl sulfate (SDS) were examined at varying amount. Three inorganic aluminium precursors, viz aluminium sulfate, aluminium nitrate and aluminium chloride, were used as the substitution aluminium sources to aluminium isopropoxide. The MAs synthesized were characterized using thermogravimetry – differential thermal analysis (TG–DTA) for decomposition and mass loss characteristics upon calcination, X-ray diffraction (XRD) for bulk crystallinity, transmission electron microscopy (TEM) for nano-scale morphology and N_2 physisorption techniques for porous structural properties. For a given SDA, increasing the amount of surfactant addition markedly improved the porosity of the MA synthesized. In terms of the ability to influence the structural properties of the resulting MAs such as BET surface area, pore volume and pore size, the SDAs tested followed a descending order of F127 > P123 > CTAB > SDS. MAs with the greatest pore volumes and pore sizes with narrow PSDs were obtained when the doping ratios of $Al(NO_3)_3$, $AlCl_3$ and $Al_2(SO_4)_3$ were 15%, 30% and 2%, respectively. Depending on the type and addition amount of SDA and the aluminium precursor composition, the BET surface area, pore volume and pore size of MAs could be adjusted in the ranges of 178 m^2g^{-1} ~ 358 m^2g^{-1}, 0.4 cm^3g^{-1} ~ 1.9 cm^3g^{-1} and 5.5 nm ~ 30.1 nm, respectively.

Keywords: Mesoporous alumina; sol-gel; structural properties

1. Introduction

Synthesis of mesoporous alumina (MAs) with controlled structural properties including BET surface area, pore volume and pore size has been the subject of intensive academic and industrial research driven by their wide applications in various fields such as catalysis, adsorption and separation, and sensing [1-3]. This is ascribed to their crystalline framework, intrinsic acidic–basic characteristics and controllable structural properties. The synthesis of MA with adjustable mesoporous structure has been a long-standing goal and many synthesis routes have been developed. Among them, the sol–gel process is regarded as one of the most promising approach [4-6]. It involves complicated organic–inorganic assemblies using surfactants as structure-directing agents (SDAs) to form a hybrid organic–inorganic mesophase by simultaneous condensation of Al ions and self-assembly of surfactant molecules [3,7]. Upon the hydrolysis of alumina precursor in the presence of a surfactant, the formation of an intermediate boehmite/surfactant nanocomposite is expected to occur. This process has attracted a great deal of attention due to its easily accessible and reproducible characteristics in fabricating MA. Moreover, it allows the control of pore size and surface area by adjusting the synthesis variables [5].

Up to now, most of the sol–gel process has been conducted using the non-ionic triblock copolymer P123 as the template in ethanol [6,8-9]. The structural properties of the resulting MAs strongly depend on the properties of the intermediate boehmite/surfactant composites assembled by Al-containing species and SDA molecules [10]. P123 is an amphiphilic molecule which belongs to the poly(ethylene oxide)–poly(propylene oxide)–poly(ethylene oxide) PEO – PPO – PEO family. In this synthesis system, P123 molecules can self-assemble to form micelles consisting of a PPO core and a corona with hydrated PEO segments and then adsorb onto the Al nanoparticle surface to form

70 the densely packed layers [10]. Although there have been numerous reports on the synthesis of MAs
71 via the sol–gel process, the SDA employed has been largely limited to the non-ionic triblock
72 copolymer P123, the use of new non-ionic SDAs as well as cationic and anionic SDAs has been
73 rarely reported.
74 Recently, a major improvement has been made by using water as the synthesis medium and,
75 consequently, crystalline mesoporous γ-Al_2O_3 with high surface areas has been achieved [3-4,7].
76 The sol–gel process conducted in the aqueous medium has the advantage of producing colloidal sols
77 with varying viscosity and high stability, which would be of interest and potential for large-scale
78 production [7].
79 In the authors' previous work using the sol–gel route in an aqueous system [11], the structural
80 properties of MA were modulated through the manipulation of P123 and HNO_3 additions, inorganic
81 aluminium precursor $Al(NO_3)_3$ doping ratio and calcination temperature. As a result, MAs with
82 controllable structural properties were obtained [11]. To the best of our knowledge, it is the first
83 time that the substantial enhancement of MA mesoporosity induced by the addition of metallic salts
84 together with the change in triblock copolymer has been demonstrated. Understanding the effect of
85 synthesis conditions on MA synthesis would enable the control of the mesoporosity features.
86 In the present contribution, an extended investigation into the effect of template and inorganic
87 aluminium precursor is reported in detail. Besides, the widely studied non-ionic triblock copolymer
88 P123, another template F127, belonging to the same PEO – PPO – PEO family, an amine based
89 cationic quaternary surfactant cetyltrimethylammonium bromide CTAB, and an anionic surfactant
90 sodium dodecyl sulfate SDS were studied at varying amount. In addition, three inorganic
91 aluminium precursors including aluminium sulfate, aluminium nitrate and aluminium chloride were
92 trialled with varying substitution fractions relative to the total aluminium.

2. Experimental

2.1 Materials and MA synthesis

MAs were synthesized using the previously reported recipe [11]. In brief, 2 mol of hot water (85 °C) was added to 20 mmol of aluminium (in the form of aluminium isopropoxide with or without the inorganic aluminium precursors) under vigorous stirring in a 100 mL flask (Schott Pty Ltd) for 15 min. Then, 0.097 mL HNO_3 (68%, Fluka) was added and the mixture was stirred and maintained at 85 °C for 12 h, during which the flask was kept uncovered in the first 2 h to allow the evaporation of isopropanol formed during the hydrolysis. A template was added to the sol and the mixture was kept under gentle stirring for another 12 h period at room temperature. Finally, an MA product was obtained by drying the sol in air in an electric oven operating at 70 °C for 12 h, followed by calcination at 700 °C in air for 4 h.

In order to investigate the effect of template type and addition amount on the structural properties of MA, four templates, including two non-ionic triblock copolymers P123 ($EO_{20}PO_{70}EO_{20}$, Mav = 5800, Sigma-Aldrich) and F127 ($EO_{106}PO_{70}EO_{106}$, Mav = 12600, Sigma-Aldrich), a cationic cetyltrimethylammonium bromide (CTAB, Sigma-Aldrich) and an anionic sodium dodecyl sulfate (SDS, Sigma-Aldrich) were systematically trialled at varying amount. Moreover, three inorganic aluminium precursors, including $Al(NO_3)_3{\cdot}9H_2O$, $Al_2(SO_4)_3{\cdot}14H_2O$ and $AlCl_3$ were also imposed on the synthesis method to examine the effect of aluminium precursors and the different anions. For convenience in discussion in this manuscript, the MA samples synthesized in this work are nominally denoted in a general form of MA*x*A*y*AlB, where A (P, F, C, S) refers to the template types (P123, F127, CTAB, SDS) and B (N, S, Cl) refers to the doped inorganic aluminium precursors ($Al(NO_3)_3$, $Al_2(SO_4)_3$, $AlCl_3$), respectively. For P123, *x* refers to "*x*" g of P123 while for

F127, CTAB and SDS, *x* denotes the equivalent moles of F127, CTAB and SDS per "*x*" g of P123. In addition, *y* signifies "*y*" mol% of inorganic aluminium precursor (if applicable) relative to the total 20 mmol of Al. For instance, MA0A indicates a MA sample synthesized without template. MA1P15AlN presents a MA sample prepared using 1 g of P123, 15% molar fraction (3 mmol) of $Al(NO_3)_3$ and then calcined at 700 °C. The detailed synthesis recipes and the resulting MA products are summarized in Table 1.

2.2 MA characterization

Structural parameters of MAs including the BET surface area, pore volume Vp, average pore size Da and pore size distribution (PSD) were determined from the nitrogen physisorption isotherms obtained using a Tristar 3020 volumetric analyser (Micromeritics Co. Ltd). The specific surface area was calculated from the adsorption branch using the BET method in the relative pressure (p/p_o) range of 0.05–0.3 [12]. Vp showed the total pore volume calculated from the adsorbed nitrogen amount at a relative pressure P/P_0 of 0.997 [13-14]. Da indicated the average pore diameter while Dp was defined as the peak value of the PSD curve derived from adsorption branch of the isotherm using the BJH calculation method [12-13]. Thermogravimetry–differential thermal analysis (TG-DTA) was performed on the synthesized MAs to obtain the mass loss characteristics during calcination using a thermogravimetric analyser (SDT Q600, TA Instrument), operating in air (50 $mLmin^{-1}$) with a heating rate of 5 °$Cmin^{-1}$ from 70 °C to 700 °C. TEM imaging was acquired using a JEM-2100 JEOL electron microscope equipped with LaB6 filament at 120 kV.

3. Results and discussion

MAs were successfully synthesized under aqueous acidic conditions. The aluminium sources were hydrolysed with the addition of water and the hydrolysis was promoted by the acidic environment

induced by the addition of nitric acid. Self-assembly of Al^{3+} was assisted by different amounts of surfactants P123, F127, CTAB and SDS, respectively, while the released isopropanol was evaporated out of solutions. A systematic study of the role of template type, template addition amount and inorganic aluminium precursors doping was shown as follows.

3.1 Effect of template type

The structural properties of all MA samples are summarized in Table 2. The nitrogen physisorption isotherms of MA1A, MA2A and MA4A are plotted in Fig. 1 (a, c, e) while the corresponding BJH PSD curves are shown in Fig. 1 (b, d, f). As can be seen, all the isotherms are of Type IV, which refers to mesoporous materials [9,12]. The isotherms measured on MA*x*P and MA*x*F present the H1 hysteresis loops while in the cases of MA*x*C and MA*x*S, the desorption branches decline steeply at the relative pressure of 0.5~0.6, exhibiting the characteristics of the H2 hysteresis loops. According to the IUPAC classification, a H1 hysteresis loop relates to the capillary condensation taking place in large pore channels with channel modulation [9,12]. Typically, the adsorption and desorption branches are almost perpendicular to the relative pressure axis and nearly parallel to each other. This shape is often associated with porous materials consisting of agglomerated uniform particles with narrow PSD [15]. In comparison, MA*x*C and MA*x*S samples showed Type H2 loops, indicative of the 'ink bottle' pores with narrow necks and wide bodies [16]. This suggests that MA*x*C and MA*x*S were less uniform and their agglomeration resulted in irregular porous structures [15].

Obviously, the addition of non-ionic templates F127 and P123 induced greater changes in the structural properties of the resulting MAs than the cationic template CTAB and anionic SDS did. Isotherms of MA*x*F and MA*x*P showed relatively steeper condensation steps, indicating uniform mesopore sizes. This is consistent with the results presented in Table 2, from which it is notable that

161 the pore size Da and Dp, pore volume Vp and BET surface area of MA samples using F127, P123,
162 CTAB and SDS as the templates presented in a descending order of MA*x*F > MA*x*P > MA*x*C >
163 MA*x*S (*x*=1, 2, 4). Specifically, for MA1A, the BET surface area increased from 236 m^2g^{-1} of
164 MA1S, 241 m^2g^{-1} of MA1C and 287 m^2g^{-1} of MA1P to 309 m^2g^{-1} of MA1F. The same trend can be
165 also observed over MA2A and MA4A and the highest BET surface area reached 358 m^2g^{-1} of
166 MA4F. Similarly, the largest pore volume 1.9 cm^3g^{-1} was obtained over MA4F, followed by MA4P
167 (1.8 cm^3g^{-1}), MA4C (0.6 cm^3g^{-1}) and MA4S (0.4 cm^3g^{-1}). A clear shift of the condensation steps
168 occurring in the hysteresis loops to greater relative pressures is evident in Fig. 1 (a, c, e), suggestive
169 of larger mesopores in the identical sequence of MA*x*F > MA*x*P > MA*x*C > MA*x*S. This pattern is
170 consistent with the corresponding PSD curves in Fig. 1 (b, d, f).
171 Fig. 4 shows the TG-DTA curves of MA0A, MA1A and MA1P*y*AlB. A 4-step reaction mechanism
172 has been proposed to explain the thermal transformation of nanocrystalline boehmite into alumina
173 [7,11], involving: (1) removal of physically adsorbed water at around 90 °C ~ 100 °C; (2) removal
174 of chemisorbed water up to 200 °C; (3) conversion of boehmite into transition alumina at around
175 380 °C; and (4) dehydration of transition alumina (due to the removal of residual hydroxyl groups
176 ending with crystallization in α-alumina). Evidently, the addition of SDAs had a marked effect on
177 the thermal decomposition process. For MA1P and MA1F, they showed similar TG-DTA curves. A
178 sharp exothermic peak was observed with the maxima at ca. 200 °C on the DTA curves of both
179 MA1P and MA1F, also accounting for a weight loss of about 25% and 50% in the corresponding
180 TG curves, respectively. This exothermic peak was believed to be associated with the
181 decomposition and removal of the embedded P123 and F127 [4,9]. The remaining weight loss
182 before the levelling off in the 250 °C – 400 °C range was attributed to the dehydroxylation of the
183 OH^- groups and the conversion of hydrated alumina into transitional alumina [7,10]. In comparison,

184 there were no similar peaks observed for MA0A, and instead, a gradual trend with a total weight
185 loss of 25% was presented. An analogous TG-DTA curve was found for MA1S, with only a small
186 exothermic peak occurring at around 170 °C. However, it should be noted that MA1C showed a
187 distinct TG-DTA curve. Four exothermic peaks in the 200 °C–320 °C range were clearly evident,
188 believed to be caused by the decomposition and oxidation of CTAB, which was consistent with the
189 literature report elsewhere [17]. A further analysis of the TG-DTA curves of MA1P*y*AlB will be
190 discussed in Section 3.3 below.
191 Fig. 5 shows typical TEM images of the synthesized MA samples. MA0A (Fig. 5a), prepared in the
192 absence of template, presented a dense structure with irregular shape. Similar nano-scale
193 morphology was observed for MA1C (Fig. 5f) and MA1S (Fig. 5g). These MAs were mainly
194 composed of closely packed adjacent nanoparticles. This observation was in line with their
195 structural properties shown in Table 2, where MA0A, MA1C and MA1S presented similar BET
196 surface areas, pore volumes and pore sizes. In contrast, MA1P (Fig. 5b) and MA1F (Fig. 5e)
197 displayed a lath-like or a scaffold-like configuration, though no significant ordering in the pore
198 arrangement could be observed. Such porous structure arose from the entanglement of nanolaths
199 [7].
200 Though remarkable differences in the structural properties and nano-scale morphology have been
201 observed over the MAs prepared with different templates, their XRD patterns were almost identical
202 (Fig. 5d insert). Therefore, it is considered that the addition of different SDAs in the boehmite
203 colloidal sols did not affect the crystalline microstructure of the resulting MAs. Rather, they only
204 acted on the organisation of the crystallites. This is consistent with the report by Bleta and
205 co-workers [7], where MAs prepared using P123 and F127 showed virtually the same XRD pattern.
206 Herein, all the MAs showed a highly crystalline diffraction pattern, indicating the crystallization of

207 the amorphous framework to γ-alumina (JCPDS Card No. 10-0425). Additional proof for the high
208 crystallinity was found from the HRTEM image of MA1P (Fig. 5c), where the presence of
209 crystalline nanoparticles with well-defined lattice planes can be clearly observed.
210 The self-assembly of boehmite particulates is actually a condensation process, during which the
211 cross-linked aluminium species can arrange around the SDAs to form the ordered mesophases [18].
212 The addition of surfactants can induce crystal growth following a layer-by-layer self-assembly
213 mechanism or a surfactant-induced fibre formation (SIFF) mechanism [19]. Initially, before thermal
214 treatment, the colloidal sol was composed of crystallized boehmite [7]. According to the literature
215 [11], in the absence of a template, boehmite can only form anhedral laths which assemble into a
216 compact structure upon calcination, as evidenced by the TEM image in Fig. 5a. In contrast, with the
217 aid of a template, boehmite nanocrystallites can act as "building blocks" to form a meso-structure
218 consisting of loosely stacked boehmite particles, leading to large pore volumes and pore sizes of the
219 resulting MAs. This mechanism is thought to be analogous to the formation of the
220 boehmite-surfactant "sandwich" structure, in which the template might intercalate into the boehmite
221 layers to generate a randomly packed boehmite-surfactant sandwich-like structure [4]. For the
222 non-ionic templates P123 and F127, the formation of boehmite nanorods can be ascribed to the
223 *in-situ* micelle templating mechanism, whereby the surfactant molecules self-aggregated into
224 bundle-like micelles and then act as the templates during the assembly process [20]. The
225 hydrophilic poly ethylene oxide (PEO) head groups of P123 and F127 can weakly interact with the
226 surface hydroxyl groups of boehmite layers through hydrogen bonding [4,7]. In addition, driven by
227 the weak coordination bonding, the alkylene oxide segments of P123 and F127 can form a
228 crown-ether-type complex with the boehmite particles [11,20]. Such hydrogen bonding and
229 coordination bonding can effectively induce the stacking of boehmite colloids [4].

An important note for the different impact of P123 and F127 on the structural properties of the resultant MAs is closely correlated to the length of their hydrophilic and hydrophobic chains [10,21]. F127 ($EO_{106}PO_{67}EO_{106}$) is predominantly composed of ethylene oxide (EO) chain, especially in comparison to P123 ($EO_{20}PO_{70}EO_{20}$). For F127, more hydrophilic EO chain relative to hydrophobic propylene oxide (PO) chain means a larger hydrophile-lipophile balance (HLB) value. It has been proven that an increase in the HLB value of surfactant molecules would facilitate and favour the hydrogen bonding between the EO chains and the hydroxyl group bonded to Al nanoparticles. This could then promote the degree of surfactant aggregation, and thus affect the textural development [21]. The surface area, pore volume and pore size of the MAs synthesized using a number of surfactants with different HLB values substantially increased with increasing HLB value [21]. This is consistent with the variations observed over the MA*x*F and MA*x*P samples in this study.

However, compared with the non-ionic counterparts (P123 and F127), neither the cationic template CTAB nor the anionic template SDS showed an equivalent capability in modulating the structural properties of the resulting MAs. As evidenced by the nitrogen physisorption isotherms and TEM imaging, upon the introduction of CTAB and SDS into the synthesis medium, the obtained MAs presented limited improvement in the structural properties. For instance, for MA20S with the largest addition amount of the template, only a relatively low surface area of 260 m^2g^{-1}, pore volume of 0.5 cm^3g^{-1} and pore size of 8.6 nm were attained.

Obviously, the structural properties of MAs prepared from the boehmite/surfactant aqueous system depend largely on the surfactant type. An evident and clear trend can be summarized in that the pore size, pore volume and BET surface area of MA samples using F127, P123, CTAB and SDS as the templates exhibited in the descending order of MA*x*F > MA*x*P > MA*x*C > MA*x*S (*x*=1, 2, 4). The

employment of the non-ionic surfactants P123 and F127 led to much improved structural properties compared with the cationic CTAB and anionic SDS.

3.2 Effect of template addition

The effect of template addition on the structural properties of MAs using the four templates, respectively, was also investigated. A series of MA*x*A samples were prepared accordingly. The nitrogen physisorption isotherms and the PSD curves are shown in Fig. 2 (a, c, e, g, i, k) and Fig. 2 (b, d, f, h, j, l), respectively. Table 2 summarizes the structural properties. As mentioned above, MA0A prepared without template showed very low nitrogen adsorption volume and mainly consisted of the interpenetrated particles with low regularity, which densely cohered to each other. However, with an increase in the surfactant concentration, irrespective of surfactant type, the nitrogen adsorption volume was generally enhanced, indicating a marked improvement in the porosity. The isotherms of MA*x*P and MA*x*F presented the H1 hysteresis loops, while MA*x*C and MA*x*S showed the H2 hysteresis loops. As interpreted in Section 3.1, this signifies that the agglomeration of boehmite particulates in MA*x*P and MA*x*F was more uniform and regular in porous structures. Furthermore, F127 and P123 were more capable to induce greater changes in terms of the control of structural properties of MA.

It is evident from Table 2 that the structural properties of MAs were strongly affected by the addition of P123 and F127. From MA0A to MA4P and MA4F, increasing trends in the BET surface area (from 236 m^2g^{-1} to 325 m^2g^{-1} and 358 m^2g^{-1}), Vp (from 0.4 cm^3g^{-1} to 1.8 cm^3g^{-1} and 1.9 cm^3g^{-1}), Da (from 5.2 nm to 19.3 nm and 20.8 nm) and Dp (from 7.0 to 28.2 nm and 30.1 nm) were observed, respectively. Further addition of P123 and F127 resulted in MAs with larger surface areas, pore volumes and pore sizes, which was consistent with the authors' previous work [11,22]. Moreover, the adsorption and desorption branches of the hysteresis loops for MA*x*P and MA*x*F

were nearly parallel and almost perpendicular to the relative pressure axis, suggestive of the uniformly agglomerated boehmite particulates [12,23].

However, it is worth noting that the PSD curves broadened with increasing template addition. A relatively narrow PSD could be attained when the pore size was increased from 7.0 nm for MA0A up to 28.2 nm for MA4P. But in the case of MA4F, though Dp reached 30.1 nm, the broadening was particularly evident, indicating a gradual deficiency of uniformity in the pore arrangement. This may be attributed to the micellization of the triblock copolymer surfactant, which could bring about significantly increased solution viscosity, and thus reduce the mobility of the nanoparticles and hinder the subsequent self-assembly process [24]. As a result, with increasing addition of P123 and F127, especially for MA4F, the PSD became progressively broader.

In contrast, upon the introduction of the template, MA*x*C showed a similar but much gentler trend while MA*x*S was quite stable. Specifically, from MA0A to MA4C, the BET surface area, pore volume and pore size gradually increased from 236 m^2g^{-1} to 258 m^2g^{-1}, 0.4 cm^3g^{-1} to 0.6 cm^3g^{-1} and 7.0 nm to 9.2 nm, respectively. More significant changes were observed when the CTAB content was further increased. For MA20C, the BET surface area, pore volume and pore size finally reached 319 m^2g^{-1}, 1.1 cm^3g^{-1} and 13.4 nm. However, within the identical range of the SDS addition amounts, the structural properties of MA*x*S seemed to be hovered, stuck at around 250 m^2g^{-1}, 0.5 cm^3g^{-1} and 6.0 nm, respectively. But for MA*x*S, there was no comparable strong impact of template addition on the structural properties of MA.

Fig.6 suggests that, with an increase in the template addition from MA1A to MA4A, almost the same nano-scale morphology of MA was retained. MA1P, MA4P, MA1F and MA4F displayed a lath-like or scaffold-like configuration without noticeable ordering in the pore arrangement. MA4C and MA4S still showed a similar compact structure to that of MA1C and MA1S. However, for

MA20C and MA20S, owing to the further increase in the template addition, three-dimensional interconnected scaffold-like mesostructured MAs were obtained. Hence, the abundant nanospace between the interpenetrated particles created by increased template addition could be conducive to the improvement in porosity.

3.3 Effect of inorganic aluminium precursors

$Al(NO_3)_3$, $AlCl_3$ and $Al_2(SO_4)_3$ were employed in this study to investigate the effect of the doping ratio of inorganic aluminium precursors on the structural properties of MAs. The nitrogen physisorption isotherms and corresponding PSD curves for a series of MAs with varying doping ratios are shown in Fig. 3. Increasing the fractions of $Al(NO_3)_3$ and $AlCl_3$ substitution in the total Al up to 15% and 30% led to a substantial increase in the pore volume and pore diameter, from 0.9 cm^3g^{-1} and 13.9 nm for MA1P to 1.1 cm^3g^{-1} and 22.4 nm for MA1P15AlN and then to 1.1 cm^3g^{-1} and 26.6 nm for MA1P30AlCl, with relatively narrow PSDs. A higher adsorption uptake of N_2 seen in Fig. 3a and Fig. 3c confirms the larger pore volumes of MA1P15AlN and MA1P30AlCl, while the clear shift of the capillary condensation steps to greater relative pressures signifies the increased pore sizes. However, a further rise in the doping ratios of $Al(NO_3)_3$ and $AlCl_3$ to 20% and 35% resulted in further expansion of pore size. This change also caused a significant fall in the surface area (from 287 m^2g^{-1} for MA1P to 178 m^2g^{-1} and 197 m^2g^{-1} for MA1P20AlN and MA1P35AlCl, respectively) and pore volume (from 0.9 cm^3g^{-1} to 0.7 cm^3g^{-1} and 0.8 cm^3g^{-1}) accompanied by much broader PSD curves, indicating the collapse of mesoporosity. Therefore, 15% and 30% are probably the optimal substitution ratios of $Al(NO_3)_3$ and $AlCl_3$ in terms of the controlling of the structural properties of MAs to achieve high surface area, large pore volume and expanded pore size with a narrow PSD. However, for MA1P*y*AlS, only 2% doping of $Al_2(SO_4)_3$ could be withstood by evaluating the changes in structural properties. The substitution of $Al_2(SO_4)_3$ in the total Al to 3%

gave rise to a broad and disordered PSD, suggestive of the noticeably reduced uniformity in pore arrangement.

The corresponding TG-DTA curves seen in Fig. 4 are quite similar to those of MA1P, especially for MA1P30AlCl and MA1P2AlS. The sharp exothermic peaks at around 200 °C can be explained by removal of template P123. The remaining weight loss starting from 250 °C was attributed to the transformation of Al_2O_3 from boehmite to γ phase. The characteristic feature of MA1P15AlN was an unique exothermic step centered around 135 °C, ascribed to the decomposition of $Al(NO_3)_3$. The TEM images of MA1P15AlN, MA1P30AlCl and MA1P2AlS in Fig. 7 showed the same morphology as that of MA1P (Fig. 5b) with a lath-like or a scaffold-like configuration.

Clearly, the impact of different inorganic aluminium precursors on the structural properties of MA varied greatly, depending on the precursor type and doping ratio. The role of NO_3^- in the synthesis system was reported to improve the overall acidity as a consequence of the hydrolysis of Al^{3+}, which generates H^+ [11]. Then the decreased pH facilitated the interaction between the PEO blocks and aluminium precursors and also increased the micelle size, resulting in larger pore size and pore volume. However, a further increase in acidity as a result of the doping of $Al(NO_3)_3$ over 15% may hinder the structure condensation, leading to disordered MAs.

It was reported that the radius and charge of the anions can profoundly influence the assembly process [3,9-10]. Herein, NO_3^- has a weaker complexation ability than that of Cl^- as the ionic radius of NO_3^- (206 pm) is larger than Cl^- (183 pm). Therefore, Cl^- can more strongly coordinate with Al^{3+} and consequently suppress the participation of Al^{3+} in the assembly process, thus leading to larger pore size and pore volume and possibly partial collapse of the mesostructure. On the other hand, the volatility of HCl in the synthesis system is higher than that of HNO_3, so the acidity of the $AlCl_3$ added system reduces more quickly than that of $Al(NO_3)_3$. As mentioned before, the reduction in

345 acidity can result in smaller pore size and pore volume. Therefore, the high volatility of HCl
346 compared to HNO_3 not only reduces the system acidity, thus leading to smaller pore size and pore
347 volume of the resulting MAs, but also decreases the concentration of Cl^- in the synthesis system,
348 which alleviates the coordination of Cl^- with Al^{3+}. This explains why MA1P10AlCl and
349 MA1P20AlCl showed smaller pore sizes and pore volumes than those of MA1P10AlN and
350 MA1P20AlN. Therefore, in the case of MA1P*y*AlCl, the effect of the doped $AlCl_3$ on the structural
351 properties of MAs was determined by the balance between the coordination of Cl^- with Al^{3+} and the
352 evaporation of the generated HCl.
353 With regard to MA1P*y*AlS, it was reported that the greater the precipitating capacity of the anion,
354 the more compact the alumina structure is obtained, owing to the compression of the double electric
355 layer of the primary colloidal particles [16,20]. Therefore, MAs prepared with $Al_2(SO_4)_3$ usually
356 have denser structures (normally depicted as lower pore volume and smaller pore size) than those
357 synthesized from nitrate or chloride salts, which is consistent with the structural properties of
358 MA1P*y*AlS shown in Tab 2.
359

360 ## 4. Conclusions

361 A facile route for the aqueous phase synthesis of mesoporous alumina (MA) with tunable structural
362 properties was demonstrated in this study by adjusting template type, template addition amount and
363 inorganic aluminium precursor doping ratio. MAs with surface area from 178 m^2g^{-1} to 358 m^2g^{-1},
364 pore volume from 0.4 cm^3g^{-1} to 1.9 cm^3g^{-1} and pore size from 5.5 nm to 30.1 nm were obtained.
365 Interaction between the boehmite particulates and the template was not strong enough to change the
366 intrinsic crystalline structure of boehmite, but could competently direct the loose stacking of the

boehmite particulates, resulting in the variations in the structural properties of MAs.

The non-ionic surfactants P123 and F127 were shown to more strongly influence the structural properties compared to CTAB and SDS with a given surfactant concentration, exhibiting in a descending order of F127 > P123 > CTAB > SDS. F127 showed superior capability in controlling the structural properties of the resulting MA, owing to its larger hydrophile-lipophile balance HLB value than that of P123. MA4F presented the highest surface area (358 m^2g^{-1}), pore volume (1.9 cm^3g^{-1}) and pore size (30.1 nm) under the conditions tested.

The optimal doping ratios of $Al(NO_3)_3$ and $AlCl_3$ were 15% and 30%, respectively, at which much larger pore volumes and pore sizes with narrow PSDs were obtained, while higher ratios of doping above 15% and 30% brought about quite broader PSDs as well as a significant reduction in the surface area and pore volume because of the collapse of mesoporosity. The introduction of $Al(NO_3)_3$ into the synthesis system improved the overall acidity, increased the micelle size, and resulted in larger pore size and pore volume. The impact of the doped $AlCl_3$ on the structural properties of MA was determined by a combination of factors such as the coordination of Cl^- with Al^{3+} and the evaporation of the generated HCl. In case of $Al_2(SO_4)_3$, the high precipitating capacity of SO_4^{2-} was the dominant factor, which resulted in a low doping ratio of $Al_2(SO_4)_3$ (2%) and a compact structure.

Acknowledgment

Partial financial support for this research has been provided by the Australian Research Council (ARC) under the ARC Linkage Project Scheme (LP100200135 and LP100200136). The authors acknowledge the facilities, scientific and technical assistance of the Australian Microscopy and Microanalysis Research Facility at the Centre for Microscopy, Characterization and Analysis, The

University of Western Australia, a facility funded by the university, state and Commonwealth governments. Wei Wu acknowledges the postgraduate research scholarships provided by The University of Western Australia and also the partial living stipend scholarship provided by The China Scholarship Council.

References

(1) J. Čejka, Appl. Catal. A: Gen. 254 (2003) 327-338.

(2) C Márquez‐Alvarez, J.P.P. N.Ž., J. Čejkab, Cat. Rev. - Sci. Eng. 50 (2008) 222-286.

(3) P. Alphonse, B. Faure, Microporous Mesoporous Mater. 181 (2013) 23-28.

(4) Q. Liu, A. Wang, X. Wang, P. Gao, X. Wang, T. Zhang, Microporous Mesoporous Mater. 111 (2008) 323-333.

(5) J. Aguado, J.M. Escola, M.C. Castro, B. Paredes, Microporous Mesoporous Mater. 83 (2005) 181-192.

(6) Q. Yuan, A. Yin, C. Luo, L. Sun, Y. Zhang, W. Duan, H. Liu, C. Yan, J. Am. Chem. Soc. 130 (2008) 3465-3472.

(7) R. Bleta, P. Alphonse, L. Pin, M. Gressier, M.J. Menu, Journal of colloid and interface science 367 (2012) 120-128.

(8) K. Niesz, P. Yang, G.A. Somorjai, Chem. Commun. (2005) 1986-1987.

(9) W. Cai, J. Yu, C. Anand, A. Vinu, M. Jaroniec, Chem. Mater. 23 (2011) 1147-1157.

(10) W. Cai, J. Yu, M. Jaroniec, J. Mater. Chem. 21 (2011) 9066.

(11) W. Wu, Z. Wan, W. Chen, M. Zhu, D. Zhang, Microporous Mesoporous Mater. 217 (2015) 12-20.

(12) K.S.W. Sing, Pure Appl. Chem. 57 (1985) 603-619.

(13) Z. Tian, M.A. Snyder, Langmuir 30 (2014) 9828-9837.

(14) Z. Tian, M.A. Snyder, Langmuir 30 (2014) 12411-12420.

(15) M. Marszewski, M. Jaroniec, Langmuir 29 (2013) 12549-12559.

(16) P. Bai, P. Wu, Z. Yan, X. Zhao, J. Mater. Chem. 19 (2009) 1554.

(17) D. Ramimoghadam, M.Z. Hussein, Y.H. Taufiq-Yap, Int J Mol Sci 13 (2012) 13275-13293.

418 (18) L.L. Pérez, S. Perdriau, G.t. Brink, B.J. Kooi, H.J. Heeres,I. Melián-Cabrera, Chem. Mater. 25
419 (2013) 848-855.
420 (19) H. Zhu, J.D. Riches, J.C. Barry, Chem. Mater. 14 (2002) 2086–2093.
421 (20) W. Cai, Y. Hu, J. Chen, G. Zhang, T. Xia, CrystEngComm 14 (2012) 972-977.
422 (21) V. González-Peña, C. Márquez-Alvarez, I. Díaz, M. Grande, T. Blasco, J. Pérez-Pariente,
423 Microporous Mesoporous Mater. 80 (2005) 173-182.
424 (22) W. Wu, Z. Wan, W. Chen, H. Yang, D. Zhang, Adv. Powder Technol. 25 (2014) 1220-1226.
425 (23) S.M. Grant, M. Jaroniec, J. Mater. Chem. 22 (2012) 86.
426 (24) P. Bai, P. Wu, Z. Yan, J. Zhou, X. Zhao, J. Phys. Chem. C 111 (2007) 9729–9733.
427

Table Captions

Table 1 MA labelling and corresponding synthesis conditions

Table 2 Adsorption parameters of MAs

433 **Table 1** MA labelling and corresponding synthesis conditions

Samples	Template (g)	Aluminium source (mmol)
MA0A	0	$Al(O\text{-}i\text{-}Pr)_3$ 20
MA1P	P123 1.00	$Al(O\text{-}i\text{-}Pr)_3$ 20
MA2P	P123 2.00	$Al(O\text{-}i\text{-}Pr)_3$ 20
MA4P	P123 4.00	$Al(O\text{-}i\text{-}Pr)_3$ 20
MA1F	F127 2.17	$Al(O\text{-}i\text{-}Pr)_3$ 20
MA2F	F127 4.34	$Al(O\text{-}i\text{-}Pr)_3$ 20
MA4F	F127 8.68	$Al(O\text{-}i\text{-}Pr)_3$ 20
MA1C	CTAB 0.06	$Al(O\text{-}i\text{-}Pr)_3$ 20
MA2C	CTAB 0.12	$Al(O\text{-}i\text{-}Pr)_3$ 20
MA4C	CTAB 0.25	$Al(O\text{-}i\text{-}Pr)_3$ 20
MA10C	CTAB 0.62	$Al(O\text{-}i\text{-}Pr)_3$ 20
MA20C	CTAB 1.24	$Al(O\text{-}i\text{-}Pr)_3$ 20
MA1S	SDS 0.05	$Al(O\text{-}i\text{-}Pr)_3$ 20
MA2S	SDS 0.10	$Al(O\text{-}i\text{-}Pr)_3$ 20
MA4S	SDS 0.20	$Al(O\text{-}i\text{-}Pr)_3$ 20
MA10S	SDS 0.50	$Al(O\text{-}i\text{-}Pr)_3$ 20
MA20S	SDS 1.00	$Al(O\text{-}i\text{-}Pr)_3$ 20
MA1P10AlN	P123 1.00	$Al(O\text{-}i\text{-}Pr)_3$ 18 $Al(NO_3)_3{\cdot}9H_2O$ 2
MA1P15AlN	P123 1.00	$Al(O\text{-}i\text{-}Pr)_3$ 17 $Al(NO_3)_3{\cdot}9H_2O$ 3
MA1P20AlN	P123 1.00	$Al(O\text{-}i\text{-}Pr)_3$ 16 $Al(NO_3)_3{\cdot}9H_2O$ 4
MA1P1AlS	P123 1.00	$Al(O\text{-}i\text{-}Pr)_3$ 19.8 $Al_2(SO_4)_3{\cdot}14H_2O$ 0.1
MA1P2AlS	P123 1.00	$Al(O\text{-}i\text{-}Pr)_3$ 19.6 $Al_2(SO_4)_3{\cdot}14H_2O$ 0.2
MA1P3AlS	P123 1.00	$Al(O\text{-}i\text{-}Pr)_3$ 19.4

434

		$Al_2(SO_4)_3 \cdot 14H_2O$ 0.3
MA1P10AlCl	P123 1.00	$Al(O\text{-}i\text{-}Pr)_3$ 18 $AlCl_3$ 2
MA1P20AlCl	P123 1.00	$Al(O\text{-}i\text{-}Pr)_3$ 16 $AlCl_3$ 4
MA1P30AlCl	P123 1.00	$Al(O\text{-}i\text{-}Pr)_3$ 14 $AlCl_3$ 6
MA1P35AlCl	P123 1.00	$Al(O\text{-}i\text{-}Pr)_3$ 13 $AlCl_3$ 7

435 **Table 2** Adsorption parameters of MAs

Samples	BET Surface Area (m^2g^{-1})	Pore Volume V_p (cm^3g^{-1})	D_a (nm)	D_p (nm)
MA0A	236	0.4	5.2	7.0
MA1P	287	0.9	9.5	13.9
MA2P	295	1.2	13.7	11.0
MA4P	325	1.8	19.3	28.2
MA1F	309	1.4	14.9	17.3
MA2F	348	1.6	17.7	23.2
MA4F	358	1.9	20.8	30.1
MA1C	241	0.4	5.9	8.2
MA2C	253	0.5	6.2	8.3
MA4C	258	0.6	6.7	9.2
MA10C	294	0.8	7.7	10.0
MA20C	319	1.1	10.2	13.4
MA1S	236	0.4	4.4	5.5
MA2S	249	0.4	4.6	5.6
MA4S	254	0.4	4.9	5.5
MA10S	258	0.4	5.7	7.3
MA20S	260	0.5	6.7	8.6
MA1P10AlN	258	1.0	12.5	19.7
MA1P15AlN	263	1.1	13.8	22.4
MA1P20AlN	178	0.7	14.7	28.1
MA1P1AlS	290	0.9	9.7	13.3
MA1P2AlS	309	0.9	9.3	14.0
MA1P3AlS	293	0.8	9.4	-
MA1P10AlCl	298	1.0	10.7	15.9
MA1P20AlCl	282	1.0	12.1	15.5
MA1P30AlCl	254	1.1	14.6	26.6
MA1P35AlCl	197	0.8	15.1	-

436

Figure Captions

Figure 1 Nitrogen physisorption isotherms (a, c, e) and corresponding pore size distributions (b, d, f) of MA*x*A. The isotherms for (1) MA1P, (2) MA1F, (3) MA1C, (4) MA1S, (5) MA2P, (6) MA2F, (7) MA2C, (8) MA2S, (9) MA4P, (10) MA4F, (11) MA4C and (12) MA4S were offset by 350, 700, 200, 0, 330, 850, 130, 0, 410, 1200, 170 and 0 cm^3g^{-1} STP on y axis, respectively.

Figure 2 Nitrogen physisorption isotherms (a, c, e, g, i, k) and corresponding pore size distributions (b, d, f, h, j, l) of MA*x*A. The isotherms for (1) MA0A, (2) MA1P, (3) MA2P, (4) MA4P, (5) MA1F, (6) MA2F, (7) MA4F, (8) MA1C, (9) MA2C, (10) MA4C, (11) MA10C, (12) MA20C, (13) MA1S, (14) MA2S, (15) MA4S, (16) MA10S and (17) MA20S were offset by 0, 150, 500, 1000, 200, 1000, 2000, 120, 250, 425, 120, 380, 100, 220, 350, 120 and 280 cm^3g^{-1} STP on y axis, respectively.

Figure 3 Nitrogen physisorption isotherms (a, c, e) and corresponding pore size distributions (b, d, f) of MA1P*y*AlB. The isotherms for (1) MA1P, (2) MA1P10AlN, (3) MA1P15AlN, (4) MA1P20AlN, (5) MA1P1AlS, (6) MA1P2AlS, (7) MA1P3AlS, (8) MA1P10AlCl, (9) MA1P20AlCl, (10) MA1P30AlCl and (11) MA1P35AlCl were offset by 0, 350, 750, 1280, 370, 800, 1250, 300, 750, 1250 and 1800 cm^3g^{-1} STP on y axis, respectively.

Figure 4 TG-DTA curves for MA, MA1P, MA1F, MA1C, MA1S, MA1P15AlN, MA1P2AlS and MA1P30AlCl.

Figure 5 Typical TEM images of (a) MA0A, (b) MA1P, (e) MA1F, (f) MA1C and (g) MA1S, (c) and (d) show the HRTEM image and wide-angle XRD pattern of MA1P, respectively.

Figure 6 Typical TEM images of (a) MA4P, (b) MA4F, (c) MA4C, (d) MA4S, (e) MA20C and (f) MA20S.

Figure 7 Typical TEM images of (a) MA1P, (b) MA1P15AlN, (c) MA1P2AlS and (d) MA1P30AlCl.

Figure 1

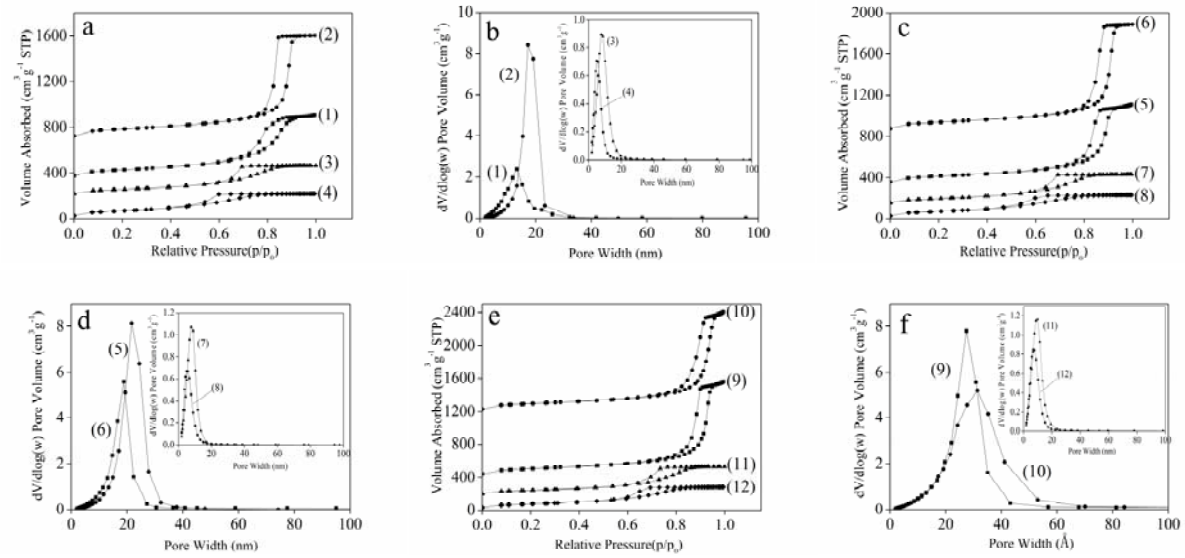

Fig. 1 Nitrogen physisorption isotherms (a, c, e) and corresponding pore size distributions (b, d, f) of MA*x*A. The isotherms for (1) MA1P, (2) MA1F, (3) MA1C, (4) MA1S, (5) MA2P, (6) MA2F, (7) MA2C, (8) MA2S, (9) MA4P, (10) MA4F, (11) MA4C and (12) MA4S were offset by 350, 700, 200, 0, 330, 850, 130, 0, 410, 1200, 170 and 0 cm^3g^{-1} STP on y axis, respectively.

1 Figure 2

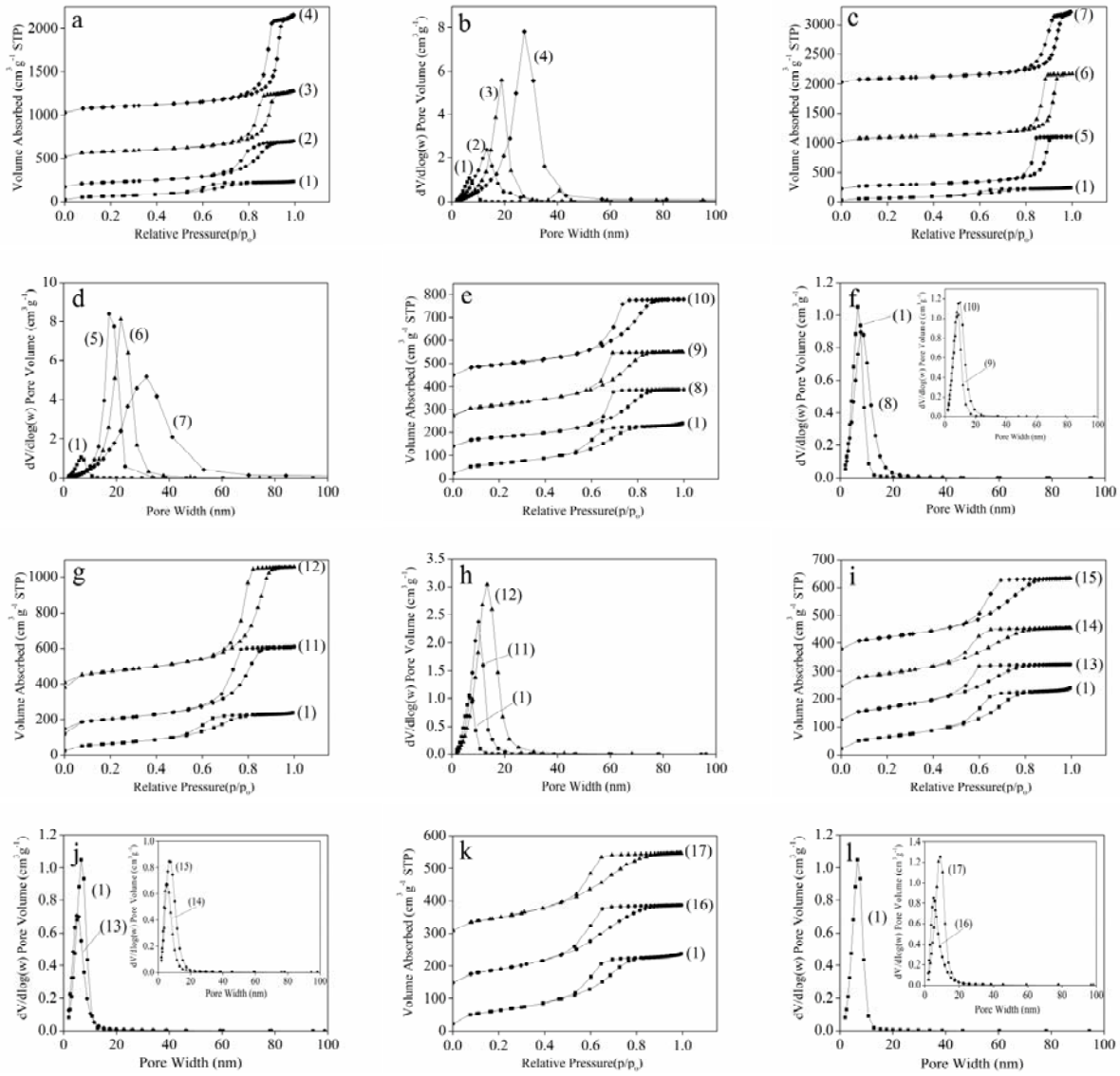
a
Volume Absorbed (cm³ g⁻¹ STP)
Relative Pressure(p/p₀)
(1)
(2)
(3)
(4)
b
dV/d(log(w) Pore Volume (cm³ g⁻¹)
Pore Width (nm)
(1)
(2)
(3)
(4)
c
Volume Absorbed (cm³ g⁻¹ STP)
Relative Pressure(p/p₀)
(1)
(5)
(6)
(7)
d
dV/d(log(w) Pore Volume (cm³ g⁻¹)
Pore Width (nm)
(1)
(5)
(6)
(7)
e
Volume Absorbed (cm³ g⁻¹ STP)
Relative Pressure(p/p₀)
(1)
(8)
(9)
(10)
f
dV/d(log(w) Pore Volume (cm³ g⁻¹)
Pore Width (nm)
(1)
(8)
(9)
(10)
g
Volume Absorbed (cm³ g⁻¹ STP)
Relative Pressure(p/p₀)
(1)
(11)
(12)
h
dV/d(log(w) Pore Volume (cm³ g⁻¹)
Pore Width (nm)
(1)
(11)
(12)
i
Volume Absorbed (cm³ g⁻¹ STP)
Relative Pressure(p/p₀)
(1)
(13)
(14)
(15)
j
dV/d(log(w) Pore Volume (cm³ g⁻¹)
Pore Width (nm)
(1)
(13)
(14)
(15)
k
Volume Absorbed (cm³ g⁻¹ STP)
Relative Pressure(p/p₀)
(1)
(16)
(17)
l
dV/d(log(w) Pore Volume (cm³ g⁻¹)
Pore Width (nm)
(1)
(16)
(17)

2

Fig. 2 Nitrogen physisorption isotherms (a, c, e, g, i, k) and corresponding pore size distributions (b, d, f, h, j, l) of MA*x*A. The isotherms for (1) MA0A, (2) MA1P, (3) MA2P, (4) MA4P, (5) MA1F, (6) MA2F, (7) MA4F, (8) MA1C, (9) MA2C, (10) MA4C, (11) MA10C, (12) MA20C, (13) MA1S, (14) MA2S, (15) MA4S, (16) MA10S and (17) MA20S were offset by 0, 150, 500, 1000, 200, 1000, 2000, 120, 250, 425, 120, 380, 100, 220, 350, 120 and 280 cm^3g^{-1} STP on y axis, respectively.

Figure 3

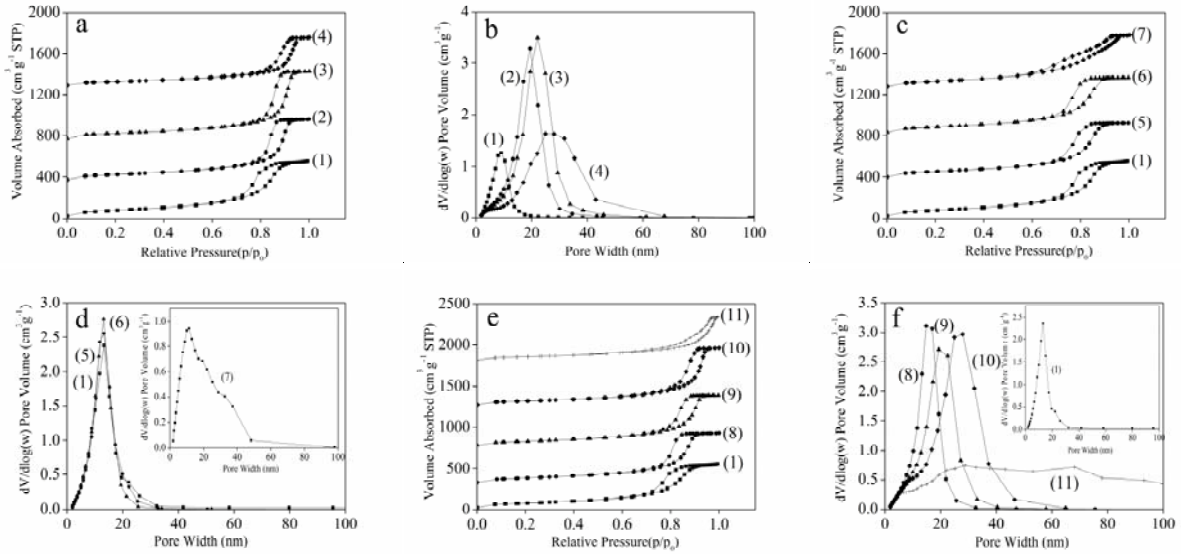

Fig. 3 Nitrogen physisorption isotherms (a, c, e) and corresponding pore size distributions (b, d, f) of MA1P*y*AlB. The isotherms for (1) MA1P, (2) MA1P10AlN, (3) MA1P15AlN, (4) MA1P20AlN, (5) MA1P1AlS, (6) MA1P2AlS, (7) MA1P3AlS, (8) MA1P10AlCl, (9) MA1P20AlCl, (10) MA1P30AlCl and (11) MA1P35AlCl were offset by 0, 350, 750, 1280, 370, 800, 1250, 300, 750, 1250 and 1800 cm^3g^{-1} STP on y axis, respectively.

1 Figure 4

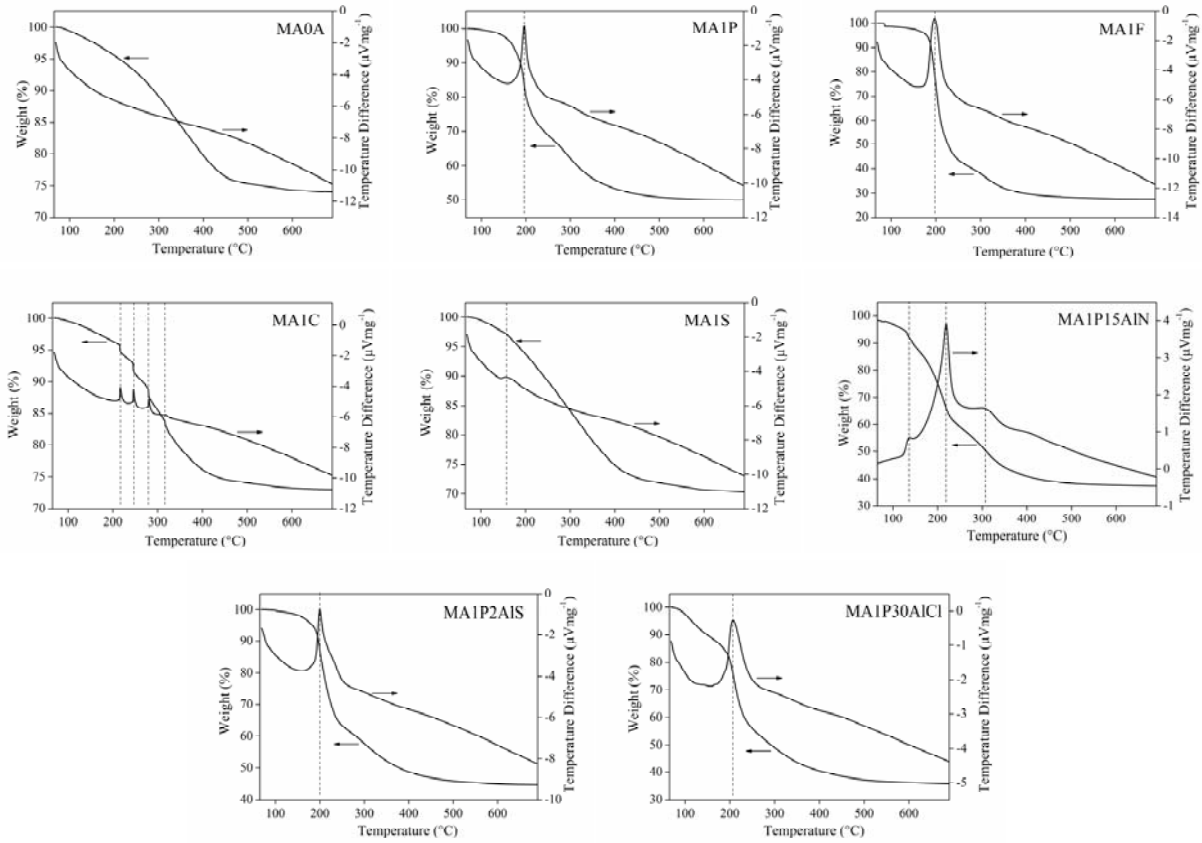

2 Fig. 4 TG-DTA curves for MA0A, MA1P, MA1F, MA1C, MA1S, MA1P15AlN,

3 MA1P2AlS and MA1P30AlCl.

Figure 5

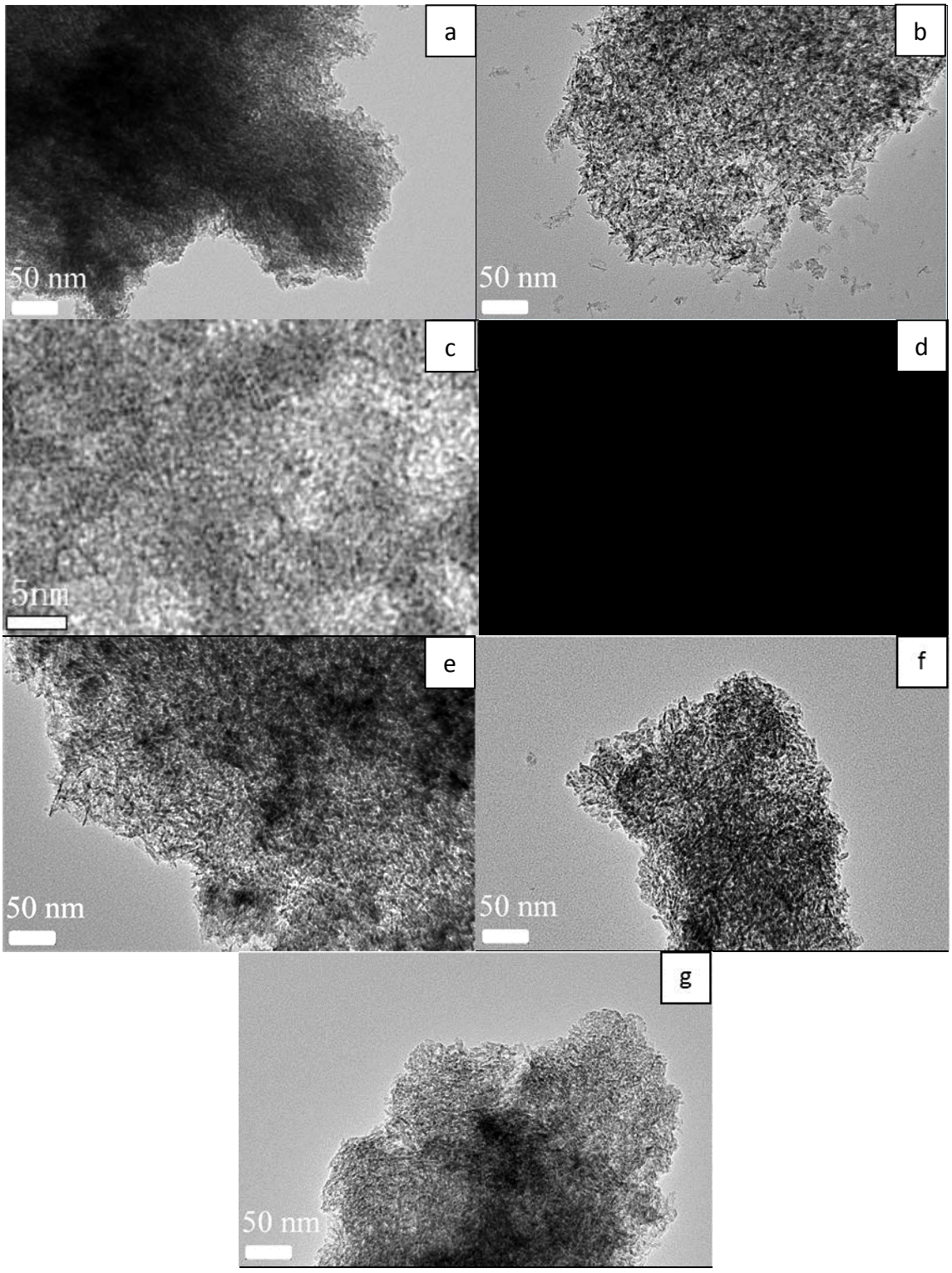

Fig. 5 Typical TEM images of (a) MA0A, (b) MA1P, (e) MA1F, (f) MA1C and (g) MA1S, (c) and (d) show the HRTEM image and wide-angle XRD pattern of MA1P, respectively.

12 Figure 6

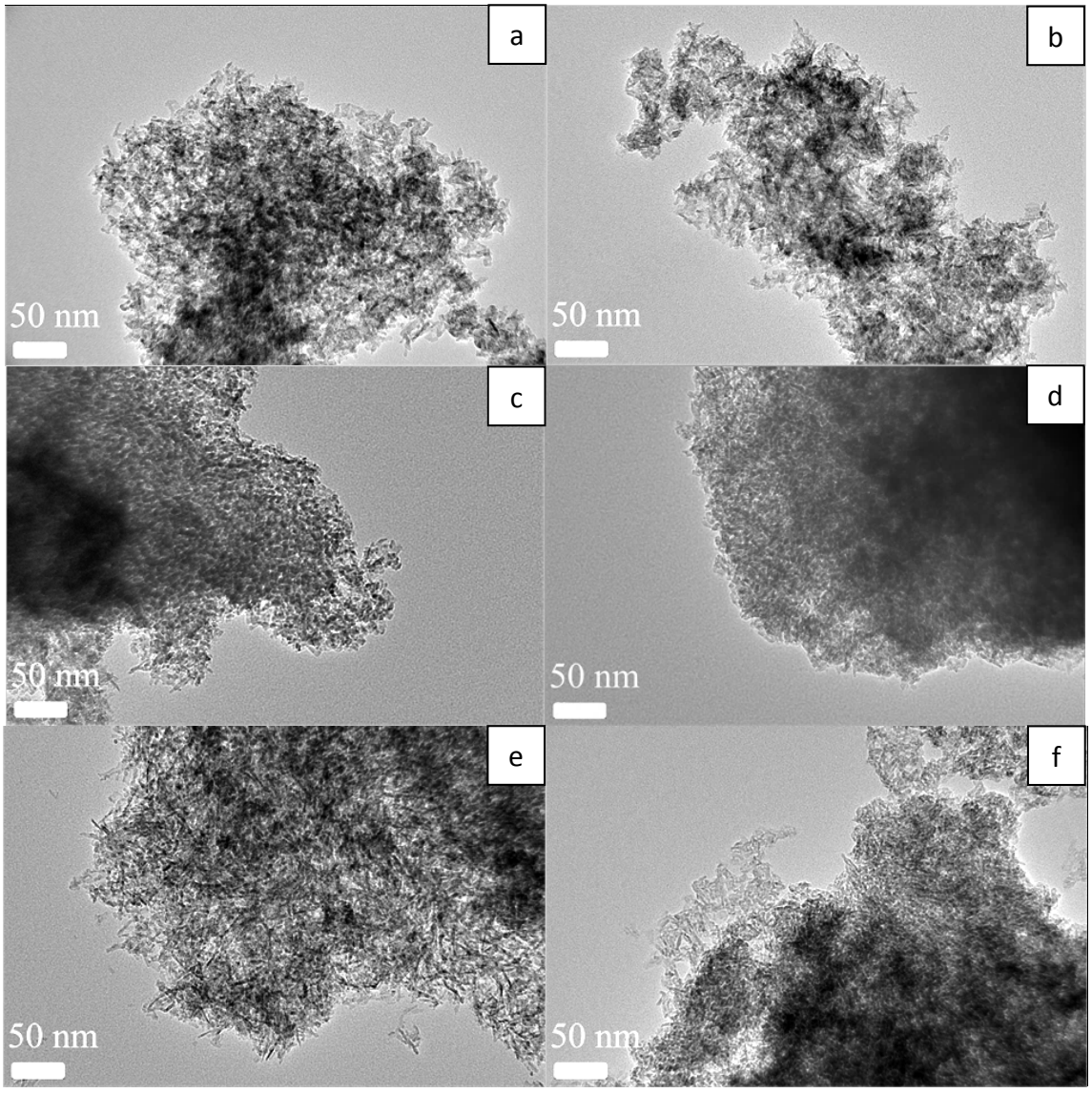

13

14

15

16 Fig. 6 Typical TEM images of (a) MA4P, (b) MA4F, (c) MA4C, (d) MA4S, (e) MA20C

17 and (f) MA20S.

Figure 7

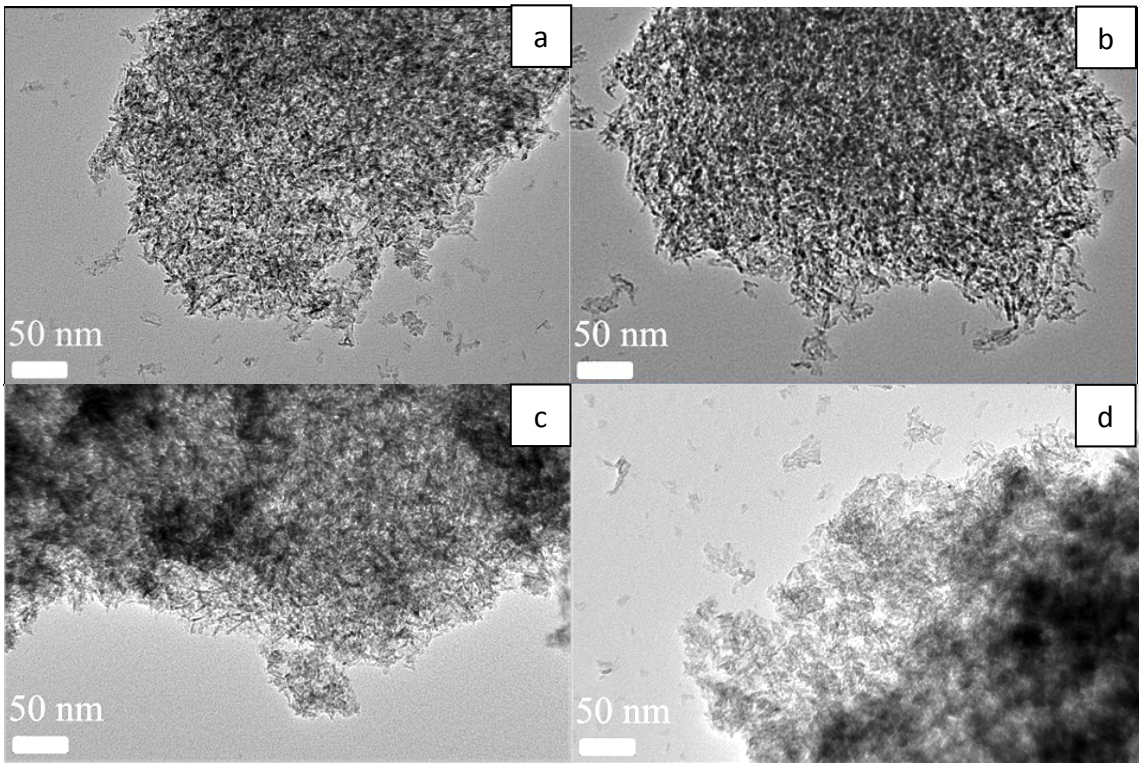

Fig. 7 Typical TEM images of (a) MA1P, (b) MA1P15AlN, (c) MA1P2AlS and (d) MA1P30AlCl.